



Global changes in oceanic mesoscale currents over the satellite altimetry record

Josué Martínez-Moreno¹✉, Andrew McC. Hogg¹, Matthew H. England^{1,2}, Navid C. Constantinou¹, Andrew E. Kiss¹ and Adele K. Morrison¹

Oceanic mesoscale eddies play a profound role in mixing tracers such as heat, carbon and nutrients, thereby regulating regional and global climate. Yet, it remains unclear how the eddy field has varied over the past few decades. Furthermore, climate model predictions generally do not resolve mesoscale eddies, which could limit their accuracy in simulating future climate change. Here we show a global statistically significant increase of ocean eddy activity using two independent observational datasets of surface mesoscale eddy variability (one estimates surface currents, and the other is derived from sea surface temperature). Maps of mesoscale variability trends show heterogeneous patterns, with eddy-rich regions showing a significant increase in mesoscale variability of 2–5% per decade, while the tropical oceans show a decrease in mesoscale variability. This readjustment of the surface mesoscale ocean circulation has important implications for the exchange of heat and carbon between the ocean and atmosphere.

Changes in the climate system over recent decades have warmed the upper ocean and modified the wind stress, heat and freshwater fluxes that drive ocean circulation^{1,2}. These changes have the capacity to modify the ocean circulation, including the overturning circulation^{3,4}, basin-scale gyres^{5,6} and boundary currents^{7,8}. Changes in climate can also affect mesoscale processes—for example, through changes in wind stress forcing over the Southern Ocean⁹. The oceanic mesoscale incorporates motions that occur at spatial scales from approximately 10 to 100 km. These motions include both steady flows (such as jets and recirculations) and time-varying flows (such as meanders and coherent vortices). Generally, time-varying mesoscale flows are also referred to as eddies. Mesoscale eddies are ubiquitous in the global ocean and feed back onto all scales, from regional processes¹⁰ up to the global meridional overturning circulation³. Moreover, these eddies transport and mix tracers such as heat, salt and nutrients^{11,12}. Understanding the evolution of the mesoscale circulation is therefore crucial to formulating better predictions of our changing oceans.

Kinetic energy (KE) quantifies the magnitude of ocean currents^{9,13–15}. KE is proportional to the square of the velocity and is commonly separated into the mean KE (MKE, computed from the time-mean velocity field) and the KE of the time-varying velocity (known as the eddy KE (EKE)). The EKE is dominated by mesoscale variability and is a substantial fraction of the total KE^{16,17}. A recent study has inferred a global increase in KE anomaly from ocean reanalyses and Argo floats¹⁵. However, these reanalyses and observations do not have the spatial resolution required to resolve the mesoscale field. Moreover, the ECCO ocean state estimate shows a slight speed-up of the currents, with a weak trend of surface KE¹⁸. In contrast, satellite observations resolve the mesoscale field at latitudes between 60°S and 60°N, and suggest that EKE in the Southern Ocean and northeastern Pacific has a robust increasing trend^{9,19–21}. However, the global multidecadal trends of mesoscale eddy activity from satellite observations are yet to be quantified.

Mesoscale flows have a footprint in both sea surface height (SSH) and sea surface temperature (SST). EKE can be directly inferred from SSH via geostrophy, and mesoscale eddies act to strain and shear the temperature field, meaning that regions of high EKE are associated with strong mesoscale SST gradients. Observed SST gradients can therefore be considered a proxy for mesoscale eddies^{22–24}.

In this study, we examine the evolution of mesoscale eddies using satellite observations of SSH and SST over the satellite altimetry record (1993–2020). We use two independent datasets—namely, altimeter SSH and National Oceanic and Atmospheric Administration Optimum Interpolated SST (v.2.1)²⁵—to estimate EKE and SST gradients, respectively (Methods). These fields are then temporally smoothed using a running average of 12 months to eliminate the seasonal cycle. The trends and the significance of each field are computed using a linear regression and a modified Mann–Kendall test²⁶ (see Methods for further details). Mesoscale variability is spatially heterogeneous; thus, we explore the trends of mesoscale eddies both globally and regionally.

Global mesoscale eddy trends

Over the past three decades, ocean thermal expansion and the melting of land ice have led to an increase in SSH^{1,27} (Fig. 1a). This SSH increase can be observed in all ocean basins, but there is also regional variability (Fig. 1b). SSH gradients are proportional to the surface geostrophic flow, from which we can compute velocity anomalies and EKE (Methods). The time-mean EKE highlights eddy-rich regions including boundary currents and their extensions, the Antarctic Circumpolar Current (ACC), and the equatorial band (Fig. 1d). These oceanic eddy-rich regions show statistically significant trends over the satellite altimetry record from 1993 to 2020 (Fig. 1f and Extended Data Fig. 1), which suggest a regional long-term adjustment of the ocean mesoscale eddy field. Moreover, the global surface area-integrated EKE has a positive trend of ~1.2% per decade (0.09 ± 0.04 PJ per m per decade; statistically significant at the 95% confidence level). The spatial structure of EKE trends is

¹Research School of Earth Sciences and ARC Centre of Excellence for Climate Extremes, Australian National University, Canberra, Australian Capital Territory, Australia. ²Climate Change Research Centre and ARC Centre of Excellence for Climate Extremes, University of New South Wales, Sydney, New South Wales, Australia. ✉e-mail: josue.martinezmoreno@anu.edu.au

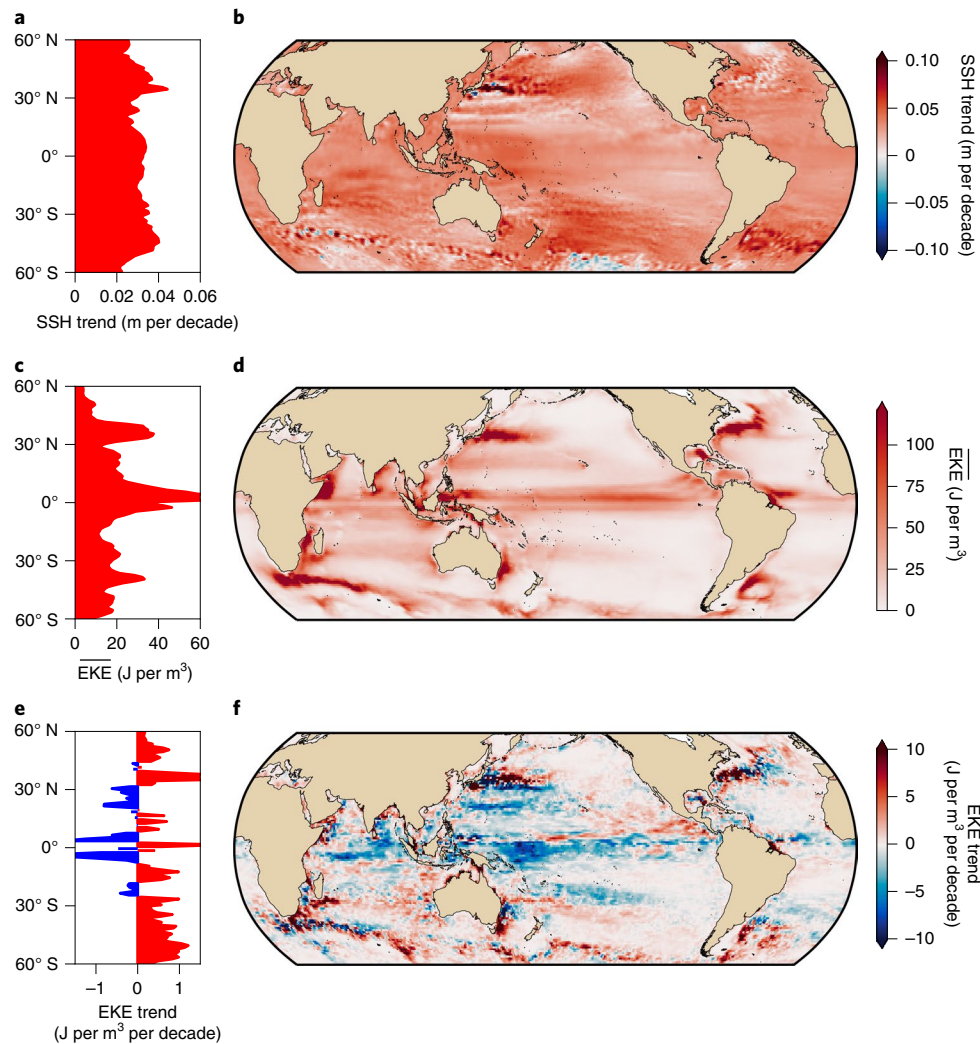


Fig. 1 | SSH trend, mean surface EKE and surface EKE trend between 1993 and 2020. **a**, Zonally averaged SSH trend. **b**, Map of SSH trend (92.1% of the area is statistically significant above the 95% confidence level; for the spatial distribution, refer to Extended Data Fig. 1a). **c**, Zonally averaged mean EKE ($\overline{\text{EKE}}$). **d**, Map of mean EKE. **e**, Zonally averaged EKE trend. **f**, Map of EKE trend (55.4% of the area is statistically significant above the 95% confidence level; see Extended Data Fig. 1b).

highly heterogeneous, although its zonal average shows notable net tendencies, with increasing trends observed polewards of 25°S and 40°N (Fig. 1e,f). A strengthening of the EKE field is a direct indication of an increase in mesoscale currents.

SST is an independent dataset relative to SSH but is also influenced by mesoscale eddies and has better temporal and spatial resolution than SSH. SST has increased on multidecadal timescales due to climate change^{28,29} (Fig. 2a), with a heterogeneous global spatial pattern modulated by interdecadal climate variability²⁸ (Fig. 2b). The time-mean SST gradients again highlight eddy-rich regions, such as boundary currents, their extensions and the ACC (Fig. 2d). These regions with large SST gradients also exhibit some of the largest positive SST gradient trends, while the subtropical gyres and the tropics mostly exhibit decreasing trends (Fig. 2e,f and Extended Data Figs. 1 and 2). The global area-integrated SST gradient magnitude has increased at a rate of $3.9 \pm 1.33 \times 10^6 \text{Cm per decade}$ or 0.2% per decade (95% confidence level) relative to the global time-mean area-integrated SST gradient magnitude ($1.7 \times 10^6 \text{Cm}$). Moreover, SST gradients are enhanced by stretching and straining due to mesoscale eddies. Further analysis shows that mesoscale SST gradients (Extended Data Fig. 3; length-scales smaller than 3° ; Methods) dominate the observed trends, increasing at a rate of

$5.37 \pm 0.94 \times 10^6 \text{Cm per decade}$ (0.4% per decade; statistically significant at the 95% confidence level). This analysis confirms that the observed SST gradient trends are a consequence of the mesoscale eddy field stirring the temperature field.

EKE and mesoscale SST gradients show analogous spatial and temporal responses in the boundary currents and their extensions, the ACC, and the tropics. Note that eddy-rich regions such as the Kuroshio Current, the Agulhas retroflection, the Gulf Stream and the East Australian Current show large changes in mesoscale SST gradients colocated with some of the largest EKE changes (Fig. 3). Even though these fields do not match perfectly, we quantified the areas of same-sign trend for each of these four regions (Extended Data Fig. 4). We find that the increasing and decreasing trends of SST and EKE match to a good extent for the Kuroshio Current, the Agulhas retroflection and the East Australian Current (61–65% of same-sign area agreement). The spatial patterns of these independent satellite products further suggest an intrinsic response of the mesoscale eddy field to a changing and variable climate.

Spatial patterns of ocean mesoscale trends

EKE and mesoscale SST gradient trends both indicate a net strengthening of the global mesoscale activity. However, both

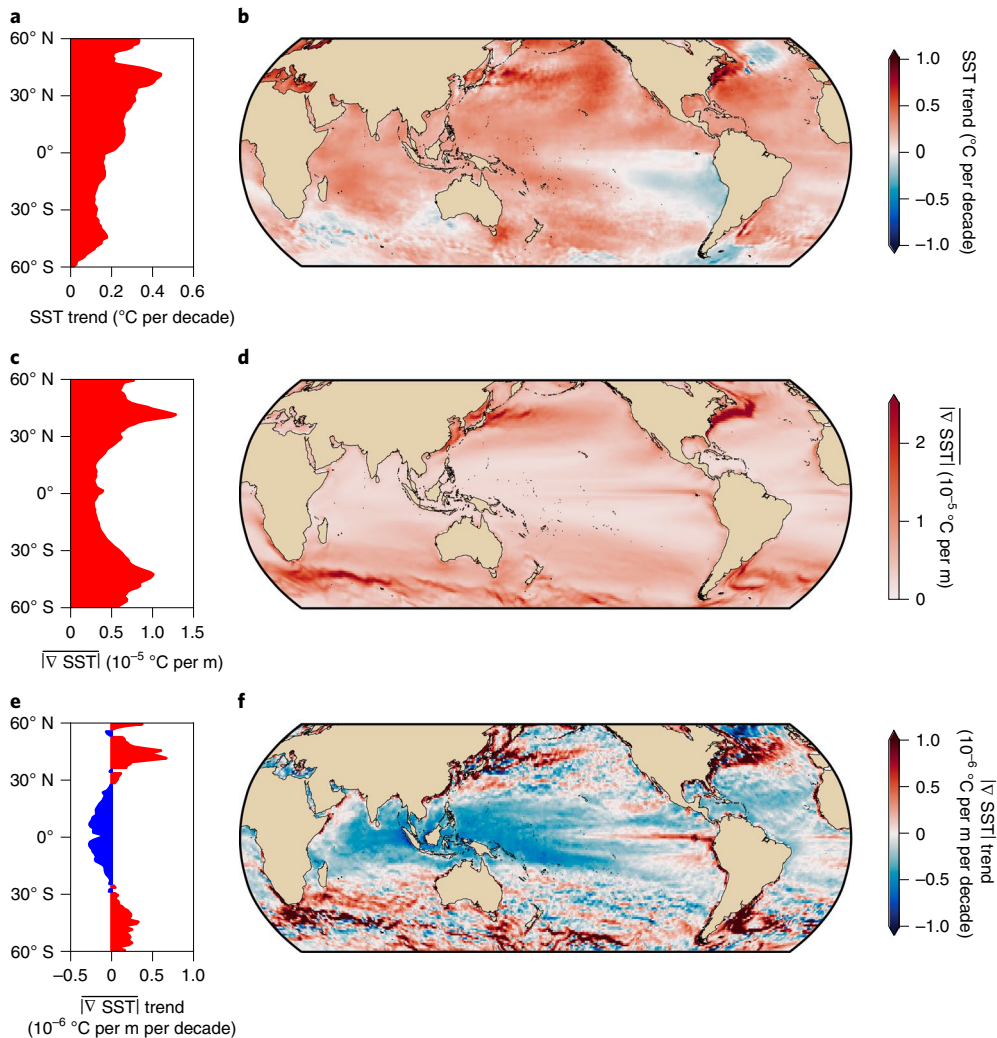


Fig. 2 | SST trends, mean SST gradient magnitude and SST gradient magnitude trends between 1993 and 2020. **a**, Zonally averaged SST trend. **b**, Map of SST trend (76.7% of the area is statistically significant above the 95% confidence level; for the spatial distribution, refer to Extended Data Fig. 1c). **c**, Zonally averaged time-mean of SST gradient magnitude ($|\nabla \text{SST}|$). **d**, Map of time-mean of SST gradient magnitude. **e**, Zonally averaged SST gradient magnitude trend. **f**, Map of SST gradient magnitude trend (81.6% of the area is statistically significant above the 95% confidence level; see Extended Data Fig. 1d). Note that the spatial pattern of SST gradient maps is independent of the temporal extent of the SST gradient record used to compute the SST gradient trends (Extended Data Fig. 2).

datasets reveal heterogeneous patterns of increasing and decreasing trends. Thus, to further understand the spatial variability, we first focus our analysis on individual area-integrated regions: namely, the Southern Ocean (by which we mean south of 35°S) and the Pacific, Indian and Atlantic Oceans north of 35°S (Fig. 4d). This analysis reveals that the Southern Ocean and the Pacific Ocean are largely responsible for the global area-integrated trends and variations of EKE and mesoscale SST gradients; the trends in the Indian and Atlantic Oceans are much smaller (Fig. 4a,b). The Southern Ocean shows a statistically significant increase for both the EKE and SST gradients, where the observed changes have been attributed to the strengthening of the wind stress since the early 1990s⁹. The Pacific Ocean SST gradient decreases significantly, with the EKE signal also decreasing, albeit below the 95% significance level (Fig. 4c,e). The large uncertainty in the Pacific EKE trend (the orange error bars in Fig. 4c) is a consequence of the pulses in the time series during 1997 and 2015, both being El Niño onset years. These large, anomalous interannual signals dominate the uncertainty of the global EKE trend.

El Niño events are associated with a strengthening of the North Equatorial Countercurrent and the northern branch of the South Equatorial Current^{30,31}, particularly during extreme eastern Pacific El Niños, such as those that occurred during 1997–1998 and 2015–2016 (ref. ³²) (the grey bars in Fig. 4a,b). During such El Niño events, the equatorial currents generate transient circulation anomalies that extend over the equatorial band (9°N–9°S). After a scale decomposition of the velocities, we observe that these EKE pulses correspond to features located in the equatorial band and have scales larger than the typical mesoscale eddy size¹¹ (approximately 10 to 100 km; Methods and Extended Data Fig. 5a,c). Thus, equatorial currents during El Niño events modulate the equatorial EKE response, and the strong interannual variability conceals EKE trends over the equatorial region.

To further investigate the effect of El Niño events on the mesoscale, we remove the equatorial regions (9°S–9°N) and repeat the global trend analysis for EKE and SST gradients. The global area-integrated extra-tropical EKE and SST gradient trends increase, while the corresponding relative uncertainties decrease; namely,

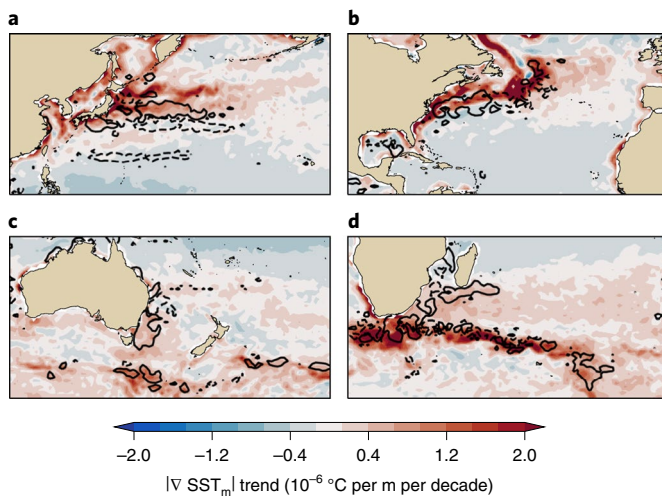


Fig. 3 | Regional maps of mesoscale SST gradient magnitude trends and surface EKE trends. **a**, Kuroshio Current. **b**, Gulf Stream. **c**, East Australian Current. **d**, Agulhas retroreflection. In all panels, the mesoscale SST gradient magnitude trends are shown by the background colour, the solid contours show positive EKE trends and the dashed contours show negative EKE trends (contours of $\pm 5 \text{ J per m}^3 \text{ per decade}$).

EKE trends are $1.8\% \pm 0.25\%$ per decade, and mesoscale SST gradient trends are $1.6\% \pm 0.09\%$ per decade (see the striped bars in Fig. 4c,e), both significant at the 95% confidence level. It is thus clear that mesoscale activity in the Pacific, and particularly in the equatorial region, is strongly influenced by interannual variability.

Eddy-rich regions become richer

The observed changes in EKE and SST of whole ocean basins integrate over large, heterogeneous regions with opposing trends. For example, the Pacific Ocean aggregates the strengthening of the equatorial currents in the equatorial Pacific Ocean during El Niño events, boundary currents and the broader-scale oceanic gyres. These dynamical regions are not unique to the Pacific Ocean; the Atlantic and Indian basins also span diverse dynamical regions. We therefore further decompose the ocean into dynamical regions (Fig. 5d): namely, (1) the ACC and surrounds, (2) the boundary currents and their extensions, (3) the equatorial regions and (4) the subtropical ocean gyres (see Methods for the dynamical region definitions). The remaining regions are aggregated into a fifth group. We then investigate the variability and trends within each of these dynamical subregions.

Globally, there is a significant increase in EKE and SST gradients; however, each dynamical region shows a different response (Fig. 5). For example, the ACC region shows a significant increase in both EKE and SST gradients at rates of 5.1% and 3% per decade (Fig. 5c,e), consistent with an increase in eddy activity with strengthening wind stress, as demonstrated in previous studies^{9,13,20}. Boundary currents and their extensions collectively show a similar net response, in which EKE and SST gradients both increase at rates of 2.5% and 8.1% per decade, respectively. Individually, SST gradients increase in all boundary currents. However, whereas EKE in the Agulhas retroreflection, the East Australian Current, the Leeuwin Current and the Malvinas Current has significantly increased, the Gulf Stream and the Kuroshio Current do not show a significant net strengthening^{33,34} (Extended Data Fig. 6); instead, regions of increase and decrease tend to cancel each other out in an area integral. This cancellation is particularly evident for the Kuroshio Current (Fig. 1f and Extended Data Fig. 6b). The response seen in the Gulf Stream and Kuroshio Current is consistent with a poleward shift in these currents^{7,35,36} and

a readjustment to climate modes³⁷. Note that a poleward shift cannot be captured by our static climatological definition of the boundary current regions (Methods). A shift of the boundary currents will thus result in an increase in EKE and SST gradients outside our dynamical definitions (that is, in regions poleward of the boundary currents and ocean gyres; see the white regions in Fig. 5d). The observed strengthening of these remaining regions is comparable to that of the ACC and suggests a poleward shift of the boundary currents, particularly in the Northern Hemisphere.

The equatorial and subtropical gyre regions exhibit statistically significant negative SST gradient trends and statistically non-significant negative EKE trends (Fig. 5), suggesting a reduction of the mesoscale eddy variability in the equatorial region and the interior of the subtropical gyres (Fig. 2). The equatorial region is dominated by interannual variability, where large changes corresponding to El Niño events occur in both the EKE and SST gradient time series. The significant decrease in SST gradients in the subtropical gyres could result from the displacement of the extratropical atmospheric circulation^{38,39} and the expansion of the tropics⁴⁰. The decreasing SST gradient trends in the tropics could be due to a homogenization of the tropical surface SST gradients. In the future, the SST gradients induced by mesoscale stirring are expected to reduce as the surface ocean becomes more thermally homogeneous. However, a longer record is required to separate the mesoscale response from interannual–decadal climate variability.

We have analysed the available satellite altimetry record of SSH and SST to reveal a significant global intensification of the mesoscale eddy field over the satellite record. While the observed global surface percentage increases per decade may seem small ($\sim 0.5\%$ per decade), like ocean heat content and sea-level trends, even small fractions of a percentage change correspond to a large energy perturbation of the Earth system. For example, if we assume that the mesoscale flow extends vertically to around 500 m in depth (a reasonable assumption given the vertical structure of the gravest mode⁴¹), then the observed EKE trends integrated over 500 m imply a significant increase of 0.78% in the global volume-integrated mesoscale energy budget ($1.3 \times 10^{19} \text{ J}$)⁴² over the satellite altimetry record after removing the El Niño signal (Extended Data Fig. 5b). This percentage is equivalent to $1.03 \times 10^{17} \text{ J}$, the same order of magnitude as the global internal tide energy budget (10^{17} J)⁴². EKE in eddy-rich regions exhibits even larger significant strengthening—for example, 2% in boundary current extensions and 5% in the ACC (Fig. 5). Increased mesoscale activity observed in both SST and mesoscale SST gradients is most apparent in regions where eddies are already strong. These eddy-rich regions are critical for carbon and heat uptake by the ocean^{43,44}, and they are known to be sensitive to climate modes that are readjusting in a changing climate—for example, the strengthening of the westerly winds⁹ linked to recent increasing trends in the Southern Annular Mode^{45,46}. With ongoing future projected changes in the westerly wind belt, it is expected that mesoscale activity in the Southern Hemisphere boundary currents and the ACC will continue to increase over the coming decades. Current generation models used for climate projections (CMIP6) do not generally resolve mesoscale eddies⁴⁷; thus, important climatic adjustments driven by changes in the eddy field are likely to be missing from these climate projections.

The mesoscale evolution described here cannot be captured by coarse-resolution reanalysis products and sparse Argo float observations, as previously used in other studies¹⁵. Here we have used eddy-permitting satellite observations to reveal a potential decrease in EKE over the tropics, while reanalysis products suggest that the tropics is where KE anomalies have increased the most¹⁵. The KE anomaly differs from EKE because it contains the time-mean flow in addition to the time-varying components. The source of differences between Hu et al.¹⁵ and our results can be assessed by an analysis of the ocean KE anomaly using satellite observations. The KE anomaly

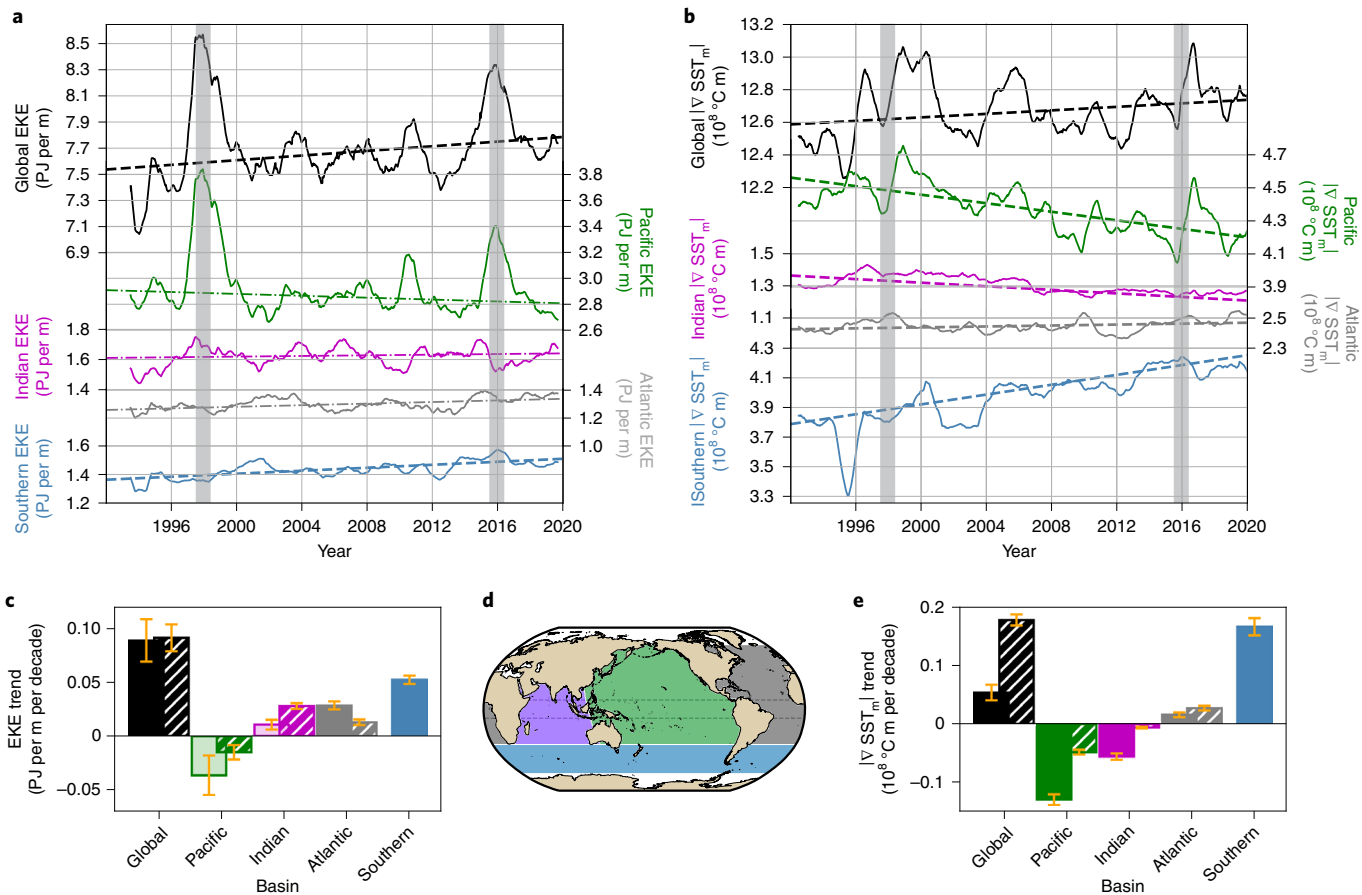


Fig. 4 | Time-series and linear trends of area-integrated surface EKE and mesoscale SST gradient magnitudes over various ocean basins. **a**, Surface EKE time series. **b**, Mesoscale SST gradient magnitude time series. In **a** and **b**, the solid curves denote 12-month running averages for each basin, the dashed lines correspond to statistically significant time-series trends, the dashed-dotted lines show statistically insignificant time-series trends and the vertical grey bars indicate El Niño events (above the 90th percentile of MEI.v2; ref. ⁴⁸). Note that the y axis is discontinuous in **a** and **b**. **c**, Linear EKE trends for each basin. **d**, Ocean basins; the equatorial region (9°S – 9°N) is marked by the dashed lines. **e**, Linear mesoscale SST gradient trends. In **c** and **e**, standard errors are shown with orange bars, and statistically significant trends (above the 95% confidence level) are solid bars, while non-significant trends are translucent. The regions are distinguished by colour: global (solid black), Southern (blue), Indian (magenta), Pacific (green) and Atlantic oceans (grey) and each region separately without the equatorial region (striped bars).

trends are almost identical to the EKE trends presented above (compare Fig. 1 and Extended Data Fig. 7), yet strikingly different from those obtained by Hu et al.¹⁵ (their Fig. 2a). This suggests that the difference between our results and those of Hu et al.¹⁵ arises from the inability of reanalyses and the Argo dataset to resolve the mesoscale, due to coarse resolution and sparse sampling, rather than from the definition of the KE anomaly. An alternative explanation of the differences between our study and Hu et al. could arise from the KE anomaly trends in Hu et al. being depth-integrated (0–2,000 m), while our EKE calculations are derived solely from surface diagnostics. In addition, as we have demonstrated, the tropics are strongly influenced by interannual variability (such as El Niño), and yet the KE time series from coarse reanalysis data does not detect the two extreme El Niño events observed in the satellite record. Data resolution and subsurface ocean dynamics are therefore the likely causes of the discrepancy between our eddy-permitting analysis and the results from prior work using reanalysis products¹⁵.

There are several possible causes of the observed trends in mesoscale activity, including (1) changes in winds (such as wind curl and wind stress), (2) changes in stratification, (3) changes in large-scale horizontal temperature gradients and (4) changes in the shear of the ocean currents. These forcing agents can impact the eddy activity via a combination of processes—for example,

the non-local intensification of winds, the outcropping and tilting of isopycnals and the strengthening of baroclinic and barotropic instability. Atmospheric reanalyses show distinct and inconsistent wind stress trend patterns, while records of in situ measurements of isopycnal tilt and baroclinic growth rate are too short and too sparse to provide evidence of a dynamical mechanism driving the observed increase in eddy activity. Longer observational records with higher temporal and spatial frequency are thus required to better understand the increase in EKE observed from satellites. In addition, as discussed above, trends computed from coarse-resolution ocean reanalysis products¹⁵ with parameterized mesoscale eddies differ from the mesoscale trends we detect from eddy-resolving satellite altimetry. An in-depth analysis of the dynamics leading to the observed mesoscale eddy evolution should therefore be explored in more detail using truly eddy-resolving global ocean models or eddy-resolving reanalysis products.

Our study has documented a major global-scale reorganization of the ocean's mesoscale KE observed over the past three decades. These observed adjustments in the mesoscale field have the potential to affect ocean circulation at regional and global scales and to modify the transport and redistribution of tracers, such as heat, carbon and nutrients. Our findings thus have major implications for

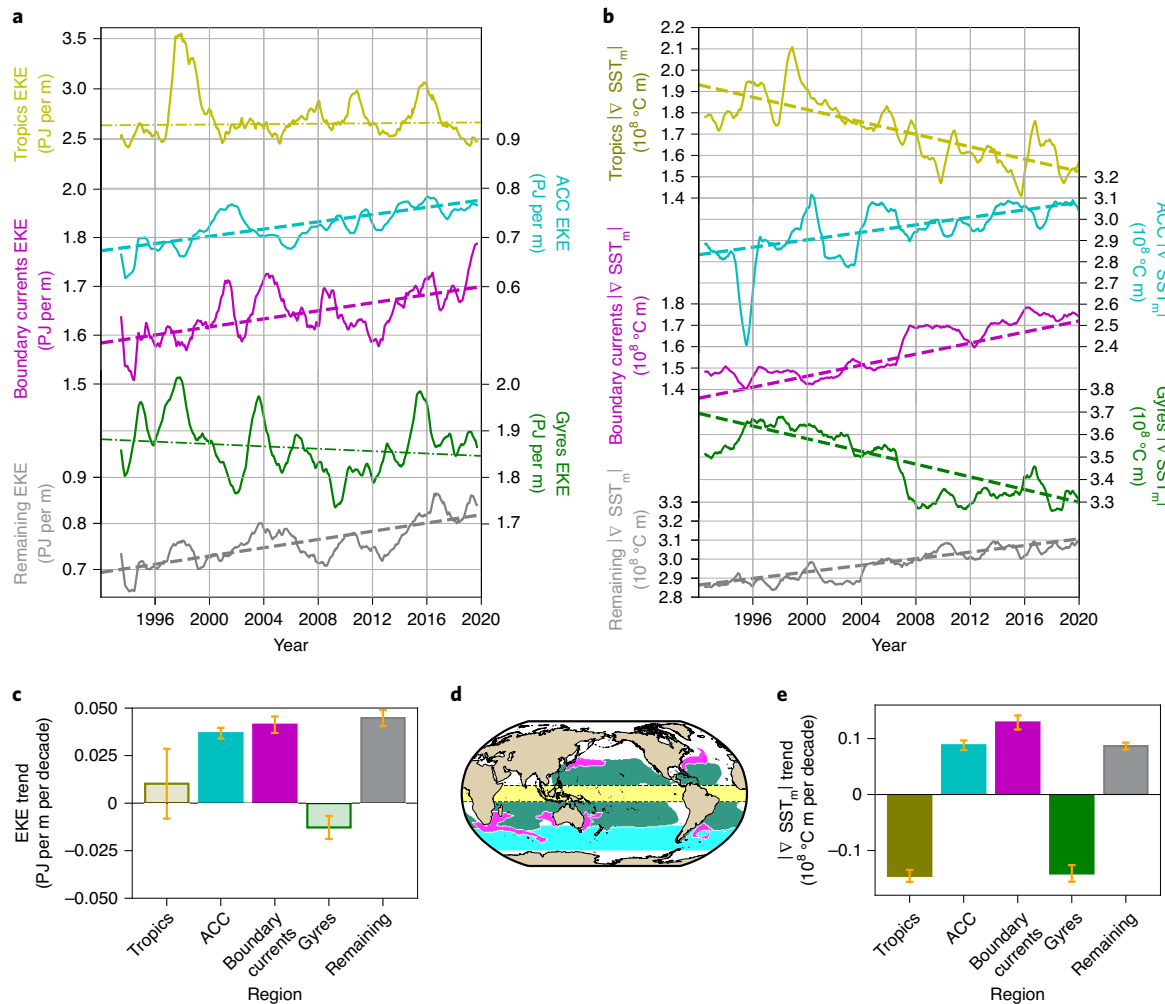


Fig. 5 | Time-series and linear trends of integrated surface EKE and mesoscale SST gradient magnitudes over dynamical regions. **a**, Surface EKE time series. **b**, Mesoscale SST gradient magnitude time series. In **a** and **b**, the solid curves are 12-month running averages for each region, the dashed lines correspond to statistically significant time-series trends and the dashed-dotted lines show insignificant time-series trends. **c**, Linear EKE trends for each dynamical region. **d**, Definition of the ocean regions. **e**, Linear mesoscale SST gradient trends. Note that in **a**, the top curve that corresponds to the tropics has a different scale than the rest. In **c** and **e**, standard errors are shown with orange bars, and statistically significant trends (above the 95% confidence level) are solid bars, while non-significant trends are translucent. The regions are distinguished by colour: tropics (yellow), ACC (cyan), boundary currents and their extensions (magenta), subtropical ocean gyres (green) and the rest (grey).

ocean readjustment to a changing climate, as the enhancement of the mesoscale ocean currents may feed back on the sequestration of anthropogenic heat and carbon into the ocean.

Online content

Any methods, additional references, Nature Research reporting summaries, source data, extended data, supplementary information, acknowledgements, peer review information; details of author contributions and competing interests; and statements of data and code availability are available at <https://doi.org/10.1038/s41558-021-01006-9>.

Received: 6 October 2020; Accepted: 11 February 2021;

Published online: 22 April 2021

References

- Pörtner, H. et al. (eds) *Special Report on the Ocean and Cryosphere in a Changing Climate* (IPCC, 2019).
- IPCC *Climate Change 2007: The Physical Science Basis* (eds Solomon, S. et al.) (Cambridge Univ. Press, 2007).
- Marshall, J., Scott, J. R., Romanou, A., Kelley, M. & Leboissetier, A. The dependence of the ocean's MOC on mesoscale eddy diffusivities: a model study. *Ocean Model.* **111**, 1–8 (2017).
- Toggweiler, J. R. & Russell, J. Ocean circulation in a warming climate. *Nature* **451**, 286–288 (2008).
- Yang, H. et al. Poleward shift of the major ocean gyres detected in a warming climate. *Geophys. Res. Lett.* **47**, e2019GL085868 (2020).
- Sutton, R. T. & Hodson, D. L. R. Climate response to basin-scale warming and cooling of the North Atlantic Ocean. *J. Clim.* **20**, 891–907 (2007).
- Wu, L. et al. Enhanced warming over the global subtropical western boundary currents. *Nat. Clim. Change* **2**, 161–166 (2012).
- Kwon, Y.-O. et al. Role of the Gulf Stream and Kuroshio–Oyashio systems in large-scale atmosphere–ocean interaction: a review. *J. Clim.* **23**, 3249–3281 (2010).
- Hogg, A. M. et al. Recent trends in the Southern Ocean eddy field. *J. Geophys. Res. Oceans* **120**, 257–267 (2015).
- Radko, T. & Marshall, J. Eddy-induced diapycnal fluxes and their role in the maintenance of the thermocline. *J. Phys. Oceanogr.* **34**, 372–383 (2004).
- Chelton, D. B., Gaube, P., Schlax, M. G., Early, J. J. & Samelson, R. M. The influence of nonlinear mesoscale eddies on near-surface oceanic chlorophyll. *Science* **334**, 328–332 (2011).
- Early, J. J., Samelson, R. M. & Chelton, D. B. The evolution and propagation of quasigeostrophic ocean eddies. *J. Phys. Oceanogr.* **41**, 1535–1555 (2011).

13. Meredith, M. P., Garabato, A. C., Hogg, A. M. & Farneti, R. Sensitivity of the overturning circulation in the Southern Ocean to decadal changes in wind forcing. *J. Clim.* **25**, 99–110 (2012).
14. Busecke, J. J. M. & Abernathey, R. P. Ocean mesoscale mixing linked to climate variability. *Sci. Adv.* **5**, eaav5014 (2019).
15. Hu, S. et al. Deep-reaching acceleration of global mean ocean circulation over the past two decades. *Sci. Adv.* **6**, eaax7727 (2020).
16. Wyrtki, K., Magaard, L. & Hager, J. Eddy energy in the oceans. *J. Geophys. Res.* **81**, 2641–2646 (1976).
17. Chelton, D. B., Schlax, M. G., Samelson, R. M. & de Szoeke, R. A. Global observations of large oceanic eddies. *Geophys. Res. Lett.* **34**, L15606 (2007).
18. Wunsch, C. Is the ocean speeding up? Ocean surface energy trends. *J. Phys. Oceanogr.* **50**, 3205–3217 (2020).
19. Patara, L., Böning, C. W. & Biastoch, A. Variability and trends in Southern Ocean eddy activity in 1/12° ocean model simulations. *Geophys. Res. Lett.* **43**, 4517–4523 (2016).
20. Martínez-Moreno, J., Hogg, A. M., Kiss, A. E., Constantinou, N. C. & Morrison, A. K. Kinetic energy of eddy-like features from sea surface altimetry. *J. Adv. Model. Earth Syst.* **11**, 3090–3105 (2019).
21. Ding, M., Lin, P., Liu, H. & Chai, F. Increased eddy activity in the northeastern Pacific during 1993–2011. *J. Clim.* **31**, 387–399 (2017).
22. Yuan, Y. & Castelao, R. M. Eddy-induced sea surface temperature gradients in eastern boundary current systems. *J. Geophys. Res. Oceans* **122**, 4791–4801 (2017).
23. Castellani, M. Identification of eddies from sea surface temperature maps with neural networks. *Int. J. Remote Sens.* **27**, 1601–1618 (2006).
24. Holladay, C. G. & O'Brien, J. J. Mesoscale variability of sea surface temperatures. *J. Phys. Oceanogr.* **5**, 761–772 (1975).
25. Banzon, V., Smith, T. M., Steele, M., Huang, B. & Zhang, H.-M. Improved estimation of proxy sea surface temperature in the Arctic. *J. Atmos. Ocean. Technol.* **37**, 341–349 (2020).
26. Yue, S. & Wang, C. The Mann–Kendall test modified by effective sample size to detect trend in serially correlated hydrological series. *Water Res. Manage.* **18**, 201–218 (2004).
27. Polito, P. S. & Sato, O. T. Global interannual trends and amplitude modulations of the sea surface height anomaly from the TOPEX/Jason-1 altimeters. *J. Clim.* **21**, 2824–2834 (2008).
28. Cane, M. A. et al. Twentieth-century sea surface temperature trends. *Science* **275**, 957–960 (1997).
29. Ruela, R., Sousa, M. C., deCastro, M. & Dias, J. M. Global and regional evolution of sea surface temperature under climate change. *Glob. Planet. Change* **190**, 103190 (2020).
30. Johnson, G. C., McPhaden, M. J., Rowe, G. D. & McTaggart, K. E. Upper equatorial Pacific Ocean current and salinity variability during the 1996–1998 Niño–La Niña cycle. *J. Geophys. Res. Oceans* **105**, 1037–1053 (2000).
31. McPhaden, M. J. The child prodigy of 1997–98. *Nature* **398**, 559–561 (1999).
32. Wang, L.-C. & Wu, C.-R. Contrasting the flow patterns in the equatorial Pacific between two types of El Niño. *Atmos. Ocean* **51**, 60–74 (2013).
33. Ezer, T., Atkinson, L. P., Corlett, W. B. & Blanco, J. L. Gulf Stream's induced sea level rise and variability along the U.S. mid-Atlantic coast: Gulf Stream induces coastal sea level rise. *J. Geophys. Res. Oceans* **118**, 685–697 (2013).
34. Uchida, H. & Imawaki, S. Estimation of the sea level trend south of Japan by combining satellite altimeter data with in situ hydrographic data. *J. Geophys. Res.* **113**, C09035 (2008).
35. Wu, B., Lin, X. & Yu, L. Poleward shift of the Kuroshio extension front and its impact on the North Pacific subtropical mode water in the recent decades. *J. Phys. Oceanogr.* **51**, 457–474 (2021).
36. Yang, H. et al. Intensification and poleward shift of subtropical western boundary currents in a warming climate. *J. Geophys. Res. Oceans* **121**, 4928–4945 (2016).
37. Piecuch, C. G. Likely weakening of the Florida Current during the past century revealed by sea-level observations. *Nat. Commun.* **11**, 3973 (2020).
38. Saenko, O. A., Fyfe, J. C. & England, M. H. On the response of the oceanic wind-driven circulation to atmospheric CO₂ increase. *Clim. Dyn.* **25**, 415–426 (2005).
39. Sen Gupta, A. et al. Projected changes to the Southern Hemisphere ocean and sea ice in the IPCC AR4 climate models. *J. Clim.* **22**, 3047–3078 (2009).
40. Seidel, D. J., Fu, Q., Randel, W. J. & Reichler, T. J. Widening of the tropical belt in a changing climate. *Nat. Geosci.* **1**, 21–24 (2007).
41. Sanchez de La Lama, M., LaCasce, J. H. & Fuhr, H. K. The vertical structure of ocean eddies. *Dyn. Stat. Clim. Syst.* **1**, dzw001 (2016).
42. Wunsch, C. & Ferrari, R. Vertical mixing, energy and the general circulation of oceans. *Annu. Rev. Fluid Mech.* **36**, 281–314 (2004).
43. Foppert, A., Donohue, K., Watts, D. & Tracey, K. Eddy heat flux across the Antarctic Circumpolar Current estimated from sea surface height standard deviation. *J. Geophys. Res. Oceans* **122**, 6947–6964 (2017).
44. Gnanadesikan, A., Pradal, M.-A. & Abernathey, R. Isopycnal mixing by mesoscale eddies significantly impacts oceanic anthropogenic carbon uptake. *Geophys. Res. Lett.* **42**, 4249–4255 (2015).
45. Abram, N. J. et al. Evolution of the Southern Annular Mode during the past millennium. *Nat. Clim. Change* **4**, 564–569 (2014).
46. Gillett, N. P. & Fyfe, J. C. Annular mode changes in the CMIP5 simulations. *Geophys. Res. Lett.* **40**, 1189–1193 (2013).
47. Haarsma, R. J. et al. High Resolution Model Intercomparison Project (HighResMIP v1.0) for CMIP6. *Geosci. Model Dev.* **9**, 4185–4208 (2016).
48. Wolter, K. & Timlin, M. S. Measuring the strength of ENSO events: how does 1997/98 rank? *Weather* **53**, 315–324 (1998).

Publisher's note Springer Nature remains neutral with regard to jurisdictional claims in published maps and institutional affiliations.

© The Author(s), under exclusive licence to Springer Nature Limited 2021

Methods

Observational products. The data used in this study include SSH, geostrophic velocities and SST. The EU Copernicus Marine Service Information (CMEMS) gridded multimission SSH and geostrophic velocities have a horizontal resolution of 1/4° (although the effective resolution may be coarser in some regions¹¹). Currents in the equatorial region (5°S–5°N) are estimated using an equatorial β-plane approximation of the geostrophic equations¹⁹. National Oceanic and Atmospheric Administration Optimum Interpolation SST has a horizontal resolution of 1/4° (ref. ²⁵). This dataset is constructed by combining observations from different products (such as satellites, ships, buoys and Argo floats).

These datasets have a quasi-global coverage (65°S–65°N) and span 27 years, from January 1993 to March 2020. The SST product is available for a longer duration, but we analyse only the period of overlap with the altimetry record (Extended Data Fig. 2). Anomalies were computed with respect to the record's climatology. We have verified that using a different period for defining the climatology does not change the observed trends in the anomaly fields. We have also verified through wavelet analysis of the time series at individual points that there is no evidence that steps in the record occurred due to improved technology in satellite missions and oceanographic observations.

KE decomposition. KE density is decomposed into the energy density contained by the steady flow (time-mean) and that contained by the transient flow (time-varying). In other words, the surface geostrophic velocity components are split using a Reynolds decomposition into their time-mean (\bar{u} , \bar{v}) and time-varying components ($u' = u - \bar{u}$, $v' = v - \bar{v}$), with bars denoting time-averages over the whole record. The terms u' and v' are the anomalies of the surface geostrophic velocities provided by CMEMS, which are proportional to the SSH gradients (via the geostrophic approximation and equatorial β-plane approximation). The KE is therefore decomposed as:

$$\underbrace{\frac{1}{2}\rho_0(u^2 + v^2)}_{\text{KE}} = \underbrace{\frac{1}{2}\rho_0(u'^2 + v'^2)}_{\text{EKE}} + \underbrace{\frac{1}{2}\rho_0(\bar{u}^2 + \bar{v}^2)}_{\text{MKE}} + \underbrace{\rho_0(\bar{u}u' + \bar{v}v')}_{\text{Cross terms}}, \quad (1)$$

where we approximate the density of the seawater by the constant $\rho_0 = 1,025 \text{ kg m}^{-3}$. The energy contained in the time-varying component of the flow is known as the EKE, while the MKE is the energy of the time-mean flow.

Maps of EKE in this study correspond to the time-mean EKE, defined as

$$\overline{\text{EKE}}(x, y) = \frac{1}{2}\rho_0(u'^2 + v'^2), \quad (2)$$

where the units of $\overline{\text{EKE}}(x, y)$ are J m^{-3} . Time series correspond to the surface area-integrated EKE (globally or over specific regions):

$$\langle \text{EKE} \rangle(t) = \iint_A \frac{1}{2}\rho_0(u'^2 + v'^2) \, dx \, dy, \quad (3)$$

where A refers to the area of each geographical or dynamical region, angle brackets $\langle \rangle$ denote the area integral and $\langle \text{EKE} \rangle(t)$ has units of J m^{-1} , as it is multiplied by the grid area.

Furthermore, the velocity field was decomposed into mesoscale (u_m , v_m ; scales smaller than 3°) and large-scale (u_{ls} , v_{ls} ; scales larger than 3°). To decompose the velocity field, we first compute u_{ls} and v_{ls} by a spatial convolution with a constant 3° × 3° kernel K :

$$\overrightarrow{u}_{ls}(x, y, t) = \frac{\iint \overrightarrow{u}(x - x', y - y', t) K(x', y') \, dx' \, dy'}{\iint K(x', y') \, dx' \, dy'}, \quad (4)$$

and the mesoscale \overrightarrow{u}_m is defined as:

$$\overrightarrow{u}_m = \overrightarrow{u} - \overrightarrow{u}_{ls}. \quad (5)$$

The mesoscale and large-scale EKE can then be computed using these velocity fields.

SST gradients. Analogous to mesoscale and large-scale EKE, SST gradients are decomposed into mesoscale (SST gradients with scales smaller than 3°) and large-scale (SST gradients with scales larger than 3°). To decompose the SST gradients, we first compute large-scale SST by using a spatial convolution with a constant 3° × 3° kernel K and a 12-month running average—that is,

$$\text{SST}_{ls}(x, y, t) = \frac{\iint \widetilde{\text{SST}}(x - x', y - y', t) K(x', y') \, dx' \, dy'}{\iint K(x', y') \, dx' \, dy'}, \quad (6)$$

where the tilde \sim denotes a 12-month running average. The mesoscale SST is then defined as

$$\text{SST}_m = \text{SST} - \text{SST}_{ls}. \quad (7)$$

The gradients of the large-scale and mesoscale SST are computed afterwards. The SST gradient magnitude is:

$$|\nabla \text{SST}| = \sqrt{\left(\frac{\partial \text{SST}}{\partial x}\right)^2 + \left(\frac{\partial \text{SST}}{\partial y}\right)^2}, \quad (8)$$

with analogous expressions for SST_m and SST_{ls} .

Computations of SST gradient time-series and time-mean SST gradient trend maps are analogous to those of EKE—for example, for the area-integrated SST gradients:

$$\langle |\nabla \text{SST}| \rangle(t) = \iint_A |\nabla \text{SST}| \, dx \, dy. \quad (9)$$

Trends, significance and uncertainties. Linear trends are calculated using a linear least-squares regression for spatially integrated time series. For the trend maps, the fields are first coarsened to a 1° × 1° grid, and then the linear trends are computed for each grid point. All the observed trends for EKE and SST gradients (time-series and trend maps) are assessed using a Theil-Sen estimator, while the statistical significance uses a modified Mann-Kendall test²⁶. This statistical test takes into account autocorrelations within the time series. Finally, the reported uncertainties in Figs. 4c,e and 5c,e correspond to the standard error using the effective sample size from the Mann-Kendall test—that is, the standard deviation of the time series divided by the square root of the effective sample size.

Geographical and dynamical regions. Geographical regions consist of the following ocean basins (Fig. 4d): the Southern Ocean (south of 35°S), the Indian Ocean, the Pacific Ocean and the Atlantic Ocean. These ocean basins were defined to capture ocean processes at all scales. The ocean basin mask can be obtained from the repository <https://doi.org/10.5281/zenodo.3993823>, which contains all the data used for this study (refer to data availability; file-name `ocean_basins_and_dynamical_masks.nc`).

Dynamical regions were defined from the climatological mean SSH and the MKE (Fig. 5d). We defined a mask for each dynamical region; then we extracted and masked each dynamical region in the following order, to avoid any overlap between regions:

1. The equatorial region is defined as the region between 9°S and 9°N.
2. The boundary currents and their extensions are defined as regions with MKE above the ~99th percentile (2.8σ). Note that the Peruvian and Californian currents are weaker (below the 99th percentile of MKE); therefore, according to our definition, they do not qualify as boundary currents.
3. The subtropical gyre masks depend on each ocean basin: the Pacific Ocean gyres correspond to mean SSH above the 0.65 m contour, the Atlantic Ocean gyres correspond to mean SSH above the 0.36 m contour and the Indian Ocean gyres correspond to mean SSH above the 0.60 m contour. All these values were tuned to approximately capture the same extension as the theoretical estimation of ocean gyres according to the Sverdrup balance.
4. The ACC and its surrounding areas is defined as all remaining regions left between 35°S and 60°S.

The dynamical regional mask can be obtained from the repository containing all the data used for this study (refer to data availability; file-name `ocean_basins_and_dynamical_masks.nc`).

Data availability

The unprocessed data from the satellite altimetry (produced by Ssalto/Duacs and distributed by EU CMEMS) can be found at https://resources.marine.copernicus.eu/?option=com_csw&view=details&product_id=SEALEVEL_GLO_PHY_I4 REP_OBSERVATIONS_008_047. The processed data used in this study are publicly available in netCDF format at <https://doi.org/10.5281/zenodo.3993823> (ref. ⁵⁰).

Code availability

All analyses and figures in this manuscript are reproducible via Jupyter notebooks and instructions found in the Github repository `EKE_SST_trends`¹¹ (<https://doi.org/10.5281/zenodo.4458783>). The analyses use the Python package `xarrayMannKendall`⁵² (<https://doi.org/10.5281/zenodo.4458776>).

References

49. Lagerloef, G. S. E., Mitchum, G. T., Lukas, R. B. & Niiler, P. P. Tropical Pacific near-surface currents estimated from altimeter, wind, and drifter data. *J. Geophys. Res. Oceans* **104**, 23313–23326 (1999).

50. Martínez-Moreno, J. et al. Eddy kinetic energy and SST gradients global datasets and trends. Additionally, this dataset includes ocean basins and ocean processes masks. *Zenodo* <https://doi.org/10.5281/zenodo.3993823> (2021).
51. Martínez-Moreno, J. & Constantinou, N. C. *josuemtzmo/EKE_SST_trends: EKE_SST_trends*: Jupyter notebooks (Python) used to compute trends of eddy kinetic energy and sea surface temperature. *Zenodo* <https://doi.org/10.5281/zenodo.4458783> (2021).
52. Martínez-Moreno, J. & Constantinou, N. C. *josuemtzmo/xarrayMannKendall: Mann Kendall significance test implemented in xarray*. *Zenodo* <https://doi.org/10.5281/zenodo.4458776> (2021).

Acknowledgements

We thank R. Holmes for clarifying the equatorial response of El Niño events during 1997–1998 and 2015–2016. The satellite altimetry products were produced by Ssalto/Duacs and distributed by CMEMS (https://resources.marine.copernicus.eu/?option=com_csw&view=details&product_id=SEALEVEL_GLO_PHY_L4 REP_OBSERVATIONS_008_047). J.M.-M. was supported by the Consejo Nacional de Ciencia y Tecnología (CONACYT), Mexico. M.H.E. was supported by the Centre for Southern Hemisphere Oceans Research (CSHOR), a joint research centre between Qingdao National Laboratory for Marine Science and Technology (QNLMT), Commonwealth Scientific and Industrial Research Organisation (CSIRO), the University of New South

Wales (UNSW) and the University of Tasmania (UTAS). A.K.M. was supported by the Australian Research Council DECRA Fellowship no. DE170100184. The analyses were undertaken on the National Computational Infrastructure in Canberra, Australia, which is supported by the Australian Commonwealth Government.

Author contributions

J.M.-M., A.McC.H. and M.H.E. conceived the study. J.M.-M. conducted the analyses. All authors contributed to the interpretation of the results and to the writing and revision of the manuscript.

Competing interests

The authors declare no competing interests.

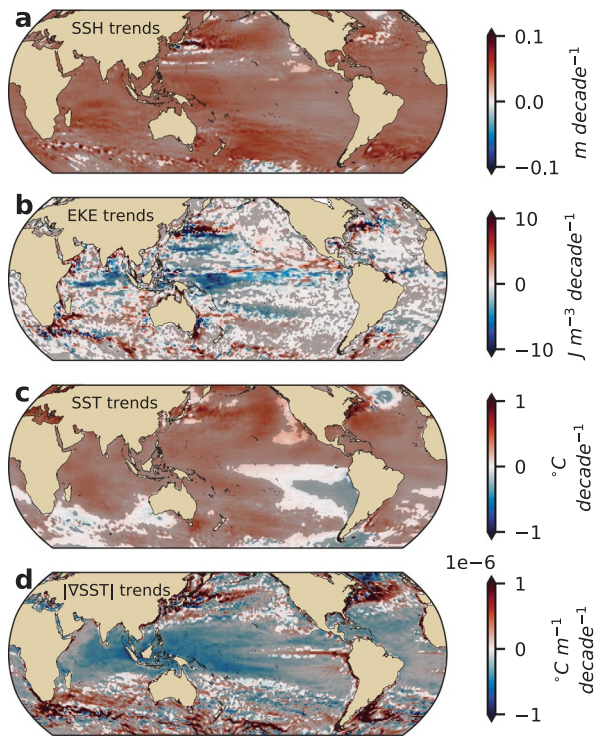
Additional information

Extended data is available for this paper at <https://doi.org/10.1038/s41558-021-01006-9>.

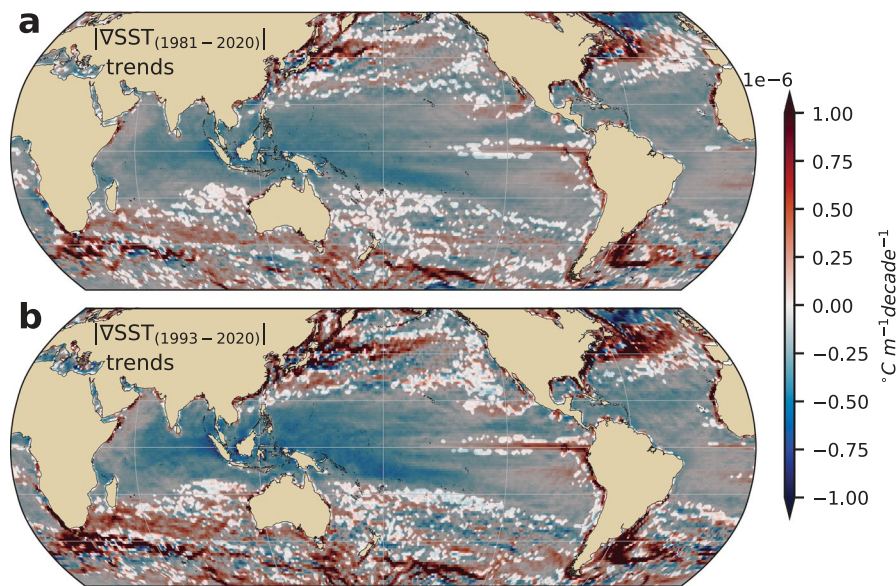
Correspondence and requests for materials should be addressed to J.M.-M.

Peer review information *Nature Climate Change* thanks Sophia Moreton and the other, anonymous, reviewer(s) for their contribution to the peer review of this work.

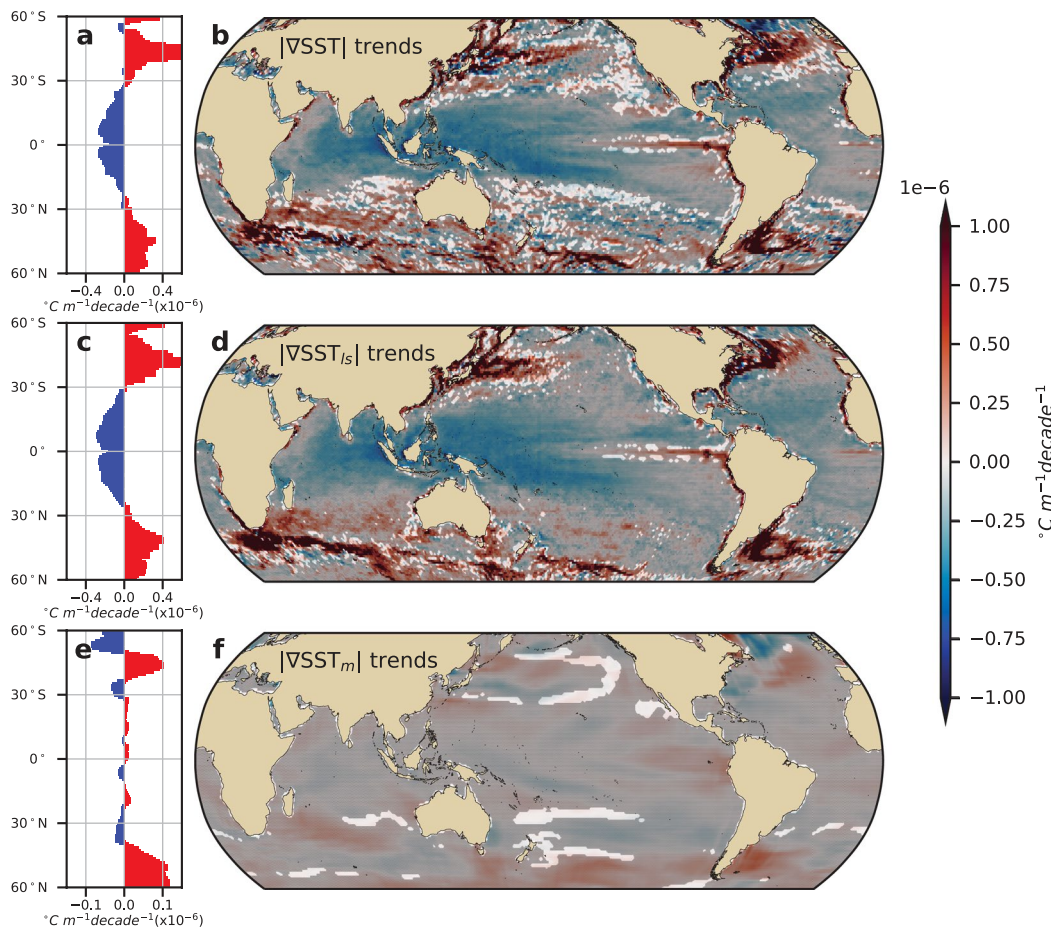
Reprints and permissions information is available at www.nature.com/reprints.



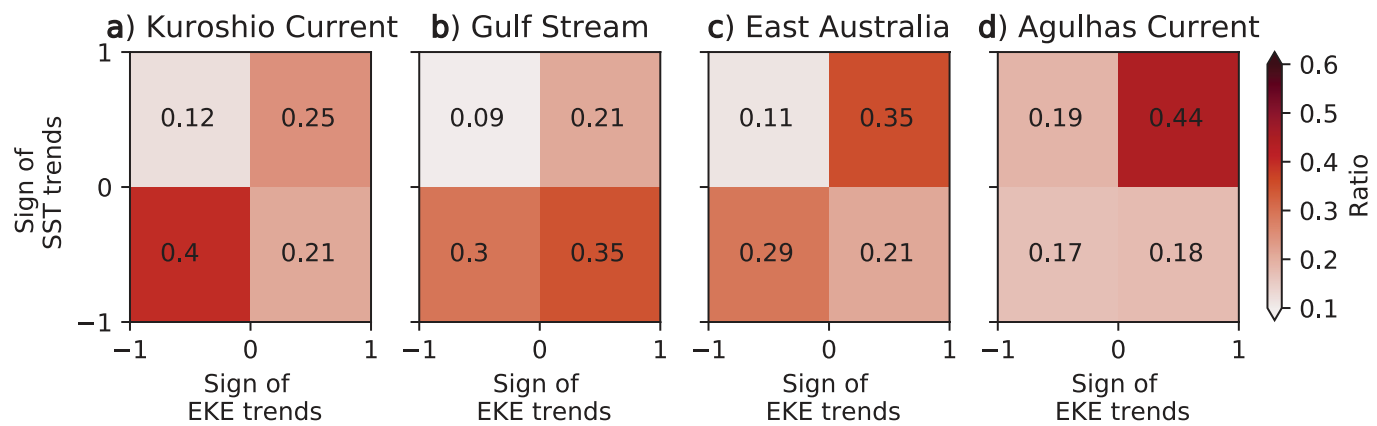
Extended Data Fig. 1 | Regions of statistically significant trends of a, sea surface height; b, surface eddy kinetic energy; c, sea surface temperature; d, sea surface temperature gradient magnitude. As per figs. 1b, f, 2b, and f in main manuscript, but showing in gray stippling regions that are statistically significant above the 95% confidence level.



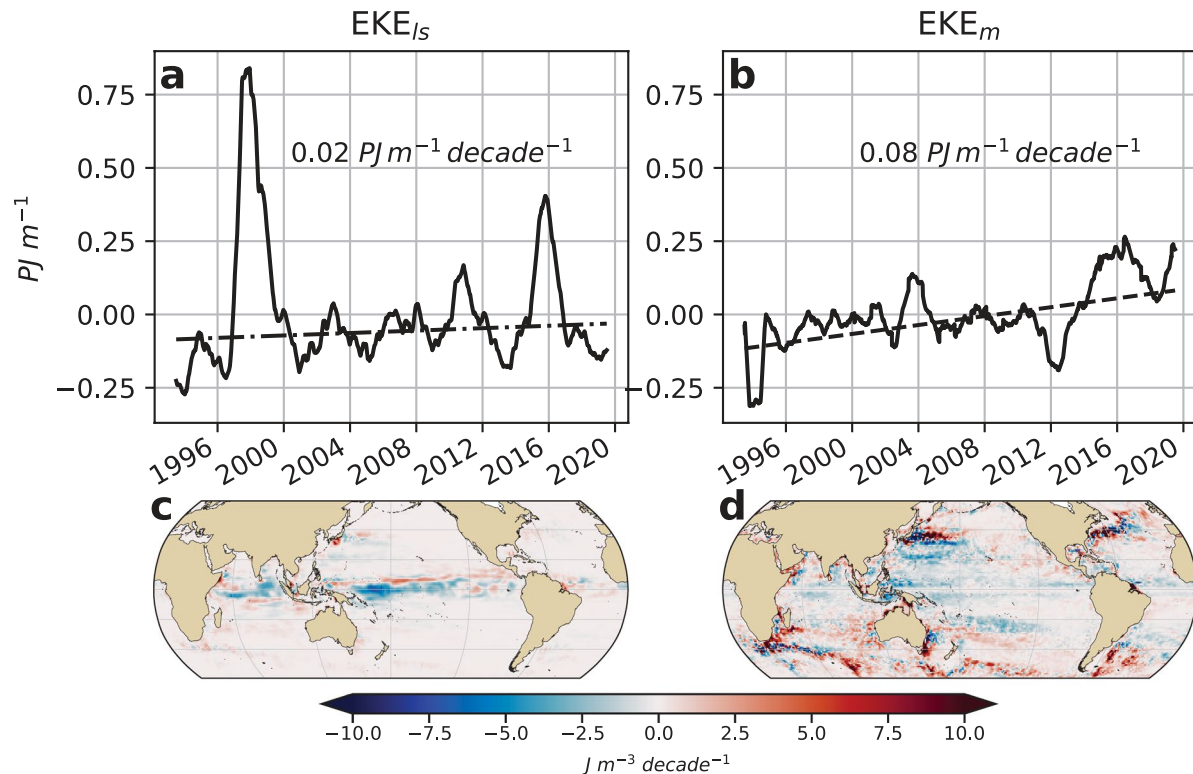
Extended Data Fig. 2 | Sea surface temperature gradient magnitude trends for periods between 1981–2020 and 1993–2020. Gray stippling shows regions that are statistically significant above the 95% confidence level.



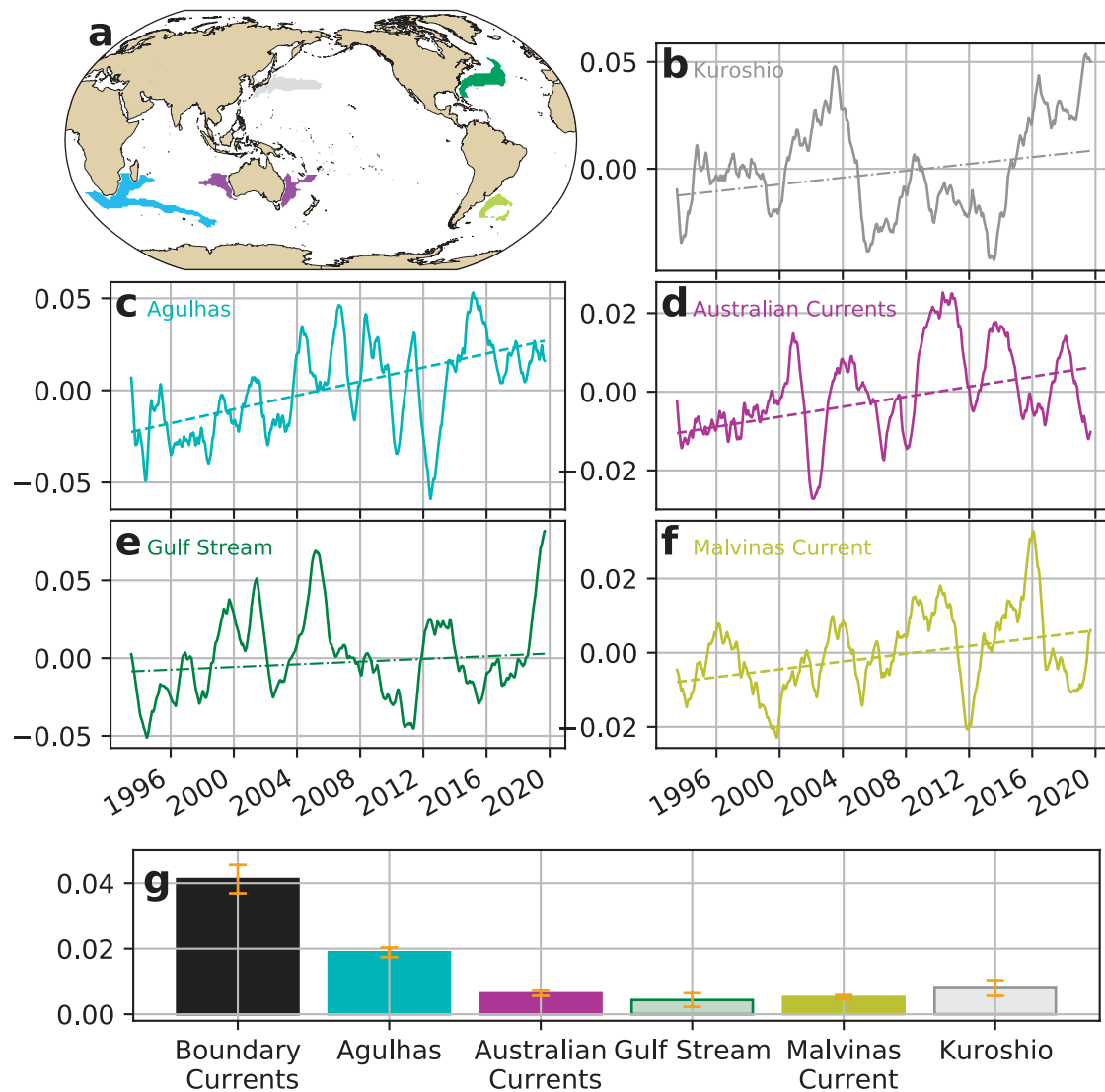
Extended Data Fig. 3 | Sea surface temperature gradient magnitude trend scale analysis. Large-scale SST gradient magnitudes are computed by filtering the SST field with a 3° kernel filter and a running average of 12 months before computing the gradient magnitudes and their respective trends (see Methods). The small scales correspond to the gradients of the SST minus the large-scale filtered SST field. **a**, Zonally averaged SST gradient magnitude trends; **b**, map of SST gradient magnitude trends; **c**, zonally averaged small-scale SST gradient magnitude trends; **d**, map of small-scale SST gradient magnitude trends; **e**, zonally averaged large-scale SST gradient magnitude trends; **f**, map of large-scale SST gradient magnitude trends. In panels **b**, **d**, and **f** gray stippling shows regions where the trends are statistically significant above the 95% confidence level.



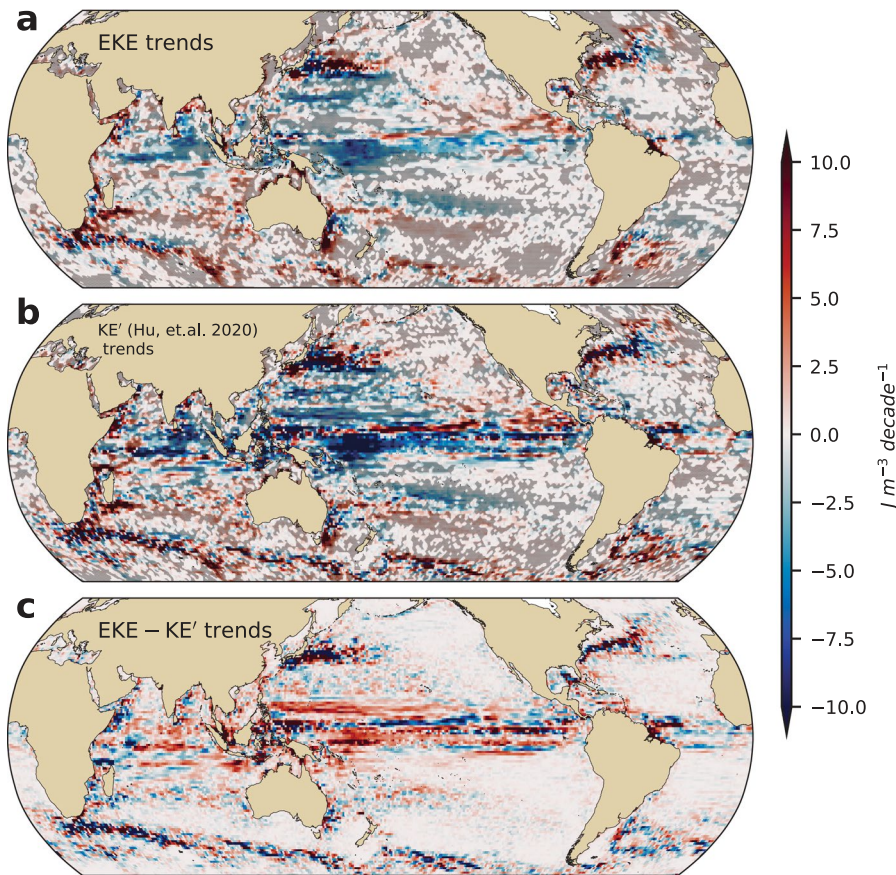
Extended Data Fig. 4 | Regional ratio of mesoscale SST gradient magnitude trends and surface EKE trends signs. **a**, Kuroshio current; **b**, Gulf Stream; **c**, East Australian Current; **d**, Agulhas retroflection. The ratio was computed by integrating the area weighted sign of the SST gradient magnitude trends and surface EKE trends divided by the total area of the region plotted in the fig. 3. Quadrants I and III of each panel show colocated regions with the same sign in SST gradients and EKE trends, more than 60% of the signs in the **a**, Kuroshio current, **c**, East Australian Current, and **d**, Agulhas retroflection are colocated.



Extended Data Fig. 5 | Surface eddy kinetic energy time-series and trends computed from filtered velocities. Scales larger than typical mesoscale are computed by filtering the surface velocity fields with a 3° kernel filter (\vec{u}'_{ls}), and the smaller scales are calculated from the difference of the velocity fields and the filtered velocity field ($\vec{u}'_m = \vec{u}' - \vec{u}'_{ls}$). Then surface EKE and their respective trends are computed (see Methods). **a**, EKE time series of scales larger than 3 degrees time series; **b**, EKE time series of scales smaller than 3 degrees; **c**, map of large-scale EKE trends; **d**, map of small-scale EKE trends. Text in panels **a** and **b** correspond to trends per decade.



Extended Data Fig. 6 | Time-series and trends of surface eddy kinetic energy integrated over boundary currents. **a**, Map of boundary current regions defined from climatological mean EKE and time series anomalies (PJ m^{-1}) and trends ($\text{PJ m}^{-1} \text{ decade}^{-1}$) for each boundary current: **b**, Kuroshio Current; **c**, Agulhas Current; **d**, East Australian Current and Leeuwin Current; **e**, Gulf Stream; **f**, Malvinas Current. **g**, Linear EKE trends for boundary currents, uncertainties are shown in orange bars and statistically significant trends (above the 95% confidence level) are denoted with solid bars while non-significant trends are translucent.



Extended Data Fig. 7 | Comparison of satellite trends using surface EKE and kinetic energy anomaly (KE') as computed by Hu et al. (2020)¹⁵. **a**, EKE trend map, **b**, KE' trend map, and **c**, difference between EKE and KE' trends. The difference between the fields is a consequence of the cross terms due to the Reynolds velocity decomposition. In panel **a** and **b** gray stippling shows regions where the trends are statistically significant above the 95% confidence level.